Dynamic Mode Decomposition of merging wind turbine wakes

Dynamic Mode Decomposition of merging wind turbine wakes

M. Zormpa[1], S. Le Clainche[2], E. Ferrer[2], C.R. Vogel[1] and R.H.J. Willden[1]

[1] University of Oxford, Department of Engineering Science, Oxford OX1 3PJ, United Kingdom
[2] Universidad Politécnica de Madrid, School of Aerospace Engineering, Plaza Cardenal Cisneros 3, E-28040 Madrid, Spain.

E-mail: markella.zormpa@eng.ox.ac.uk

Abstract. The design and operation of wind farms is significantly affected by the impact that upstream turbine wakes have on the power production and fatigue loading of subsequent turbines; often called the wake effect. In this work, two types of flows are considered: the wake of a single turbine with a laminar inflow and the combined wake of two turbines operating in-line where the upstream wake results in an unsteady inflow for the downstream turbine. Those two scenarios are simulated using large eddy simulation (LES) and the actuator line method (ALM). The spatio-temporal velocity fields are analyzed by means of high order dynamic mode decomposition (HODMD), a well established variant of the DMD. The results show that most of the higher frequencies characterizing the laminar case are instead dominated by the lower frequency modes in the combined wake. This suggests that structures emerging from the blade rotations in a wind turbine wake may be less significant for describing the wake dynamics when the rotor is operating in the unsteady wake of an upstream rotor.

1. Introduction

Moving away from carbon-intensive energy generation methods will likely require a drastic increase in the deployment of large wind farms. One of the greatest challenges when it comes to wind farm aerodynamics is the complex turbine-turbine interaction that arises from their persistent wakes. The adverse impact of these wakes on the performance of downstream turbines relative to unwaked turbines, often called the wake effect, can be significant. For example a 10-20%, reduction of average power production was attributed to the wake effect for an offshore wind farm [1]. The losses for turbines at the second row of an onshore wind farm in unstable atmospheric conditions were estimated to be 20-40%, and 40-60% under stable conditions [2]. Better understanding and modelling of the wake effect could contribute towards reducing losses of such significance.

The wake effect has been investigated in the literature by employing a number of approaches. The single turbine wake has been studied through stand-alone rotor experiments [3] as well as numerical simulations such as actuator line method large eddy simulations (ALM-LES) [4]. Understanding of single wake flow mechanisms has been incorporated into analytical models [5, 6]. However, the multi-turbine problem is more complex.

The impact of turbine clustering on power production has been observed using wind turbine operational data [1, 2]. Such results are challenging to reproduce due to the large range of

scales present in wind farm flows. Simple analytical models can fail to predict the velocity deficit and how wakes combine accurately [7], resulting in the increasing use of simulation when investigating the dynamics of multi-turbine configurations. One approach has been to use actuator disk method (ADM) simulations [8], where the rotors are represented in a disk-averaged sense, allowing the mean momentum deficit and mean power to be solved, but omitting important unsteady dynamics associated with rotating blades. Greater fidelity can be achieved using inherently unsteady ALM-LES simulations, but this is computationally prohibitive for very large wind farms due to the considerable associated computational requirements.

A further challenge when simulating large wind farms is extracting coherent structures and developing an understanding of wake evolution and merger. Dynamic mode decomposition (DMD), together with proper orthogonal decomposition (POD) are decomposition algorithms that have been used to gain insight into characteristics of turbulent flows. These algorithms analyze spatio-temporal data by decoupling spatial structures from temporal dynamics. Specifically, DMD ensures that the temporal dynamics of each mode are characterized by a single frequency. POD and DMD analysis has been applied to data-sets of various wind energy problems, including wakes, wind farm flows, and prediction of the wind resource.

By considering the wind turbine wake as a vortex system, it is possible to apply DMD to investigate the instability mechanisms of the system. Sarmast *et al.* [9] characterized the interaction between neighbouring vortex filaments for a rotor wake simulated using the ALM. Similar modes in the near wake emerge when the rotor is fully resolved in Sun *et al.* [10]. The interaction between the tip vortex systems of two rotors in tandem was investigated by Kleine *et al.* [11]. By understanding the fundamental structures of the flow downstream of a rotor, low order models can be developed [9] for the prediction of the breakdown of those structures.

DMD can also be used to identify coherent structures of turbulent flows. Bastine *et al.* [12] applied POD in ADM-LES simulations with turbulent inflow and identified wake meandering as the most energetic structures. POD analysis of ADM-LES of a very large wind farm by VerHulst and Meneveau [8] identified vortical structures much larger than the turbine scale as the most energetic modes. Debnath *et al.* [13] observed that the inclusion of the tower and nacelle in ALM-LES simulations with laminar inflow altered some of the tip vortex breakdown mechanisms identified in the case without supporting structures. De Cillis *et al.* [14] applied DMD to the flow of a wind turbine wake with and without background turbulence and concluded that in the turbulent case, the exogenous background flow dynamics prevail compared to the endogenous higher frequency dynamics of the wake. Additionally to the diagnostics, the modes can also be used to build reduced order models for the temporal prediction of the flow by either projection in the case of POD [15], or by directly using the known mode frequencies in the case of DMD [16]. Le Clainche *et al.* [17] used High Order DMD (HODMD) as a predictive tool, to spatially extrapolate velocities outside the span of available LiDAR measurements upstream a wind turbine.

This study employs DMD to explore the impact of an upstream rotor on the wake dynamics of a downstream rotor. Kleine *et al.* [11] investigated the interaction of the tip vortices of two rotors in tandem. Here, the first wake is allowed to breakdown to create an unsteady inflow to the second turbine. This is similar to De Cillis *et al.* [14], except that the source of the unsteady inflow in the present study is the upstream turbine wake. De Cillis *et al.* found that atmospheric turbulence drastically altered the dynamics of the wake when compared to the laminar inflow case. To explore how the dynamics and coherent structures in a turbine wake are affected by the presence of an upstream rotor, two data sets are generated: the spatio-temporal velocity data of the wake of a single turbine, and the wake of the second turbine, in-line and downstream of the first. The two data sets are generated using ALM-LES. Once the flow results have been validated using available experimental data, they are processed using HODMD, a flexible and efficient variant of the DMD. The dominant modes and frequencies for the two data sets are

presented and compared. Thus, the two wakes are compared in a dynamic sense.

This paper is organized as follows: in section 2 the sensitivity study and numerical results are presented. In section 3 a brief description of the HODMD algorithm is given. The DMD analysis of the two data sets is presented and discussed in section 4. Conclusions are drawn in section 5.

2. Numerical simulations

We simulate the NTNU Blind Test (BT) experimental rotor, a $D = 0.894\ m$ diameter, three bladed wind turbine with blades composed of NREL S826 aerofoils [3, 18]. The wind tunnel dimensions are $[L \times W \times H] = [11.15 \times 2.71 \times 1.8]\ m$. The inflow velocity profile is uniform and the turbulence intensity levels are low (0.3%).

The set-up and data from two experiments are used here. BT1 [3], presents data of a single wind turbine wake at various tip speed ratios (λ). Horizontal and vertical profiles of mean velocity and turbulence statistics are available at three locations downstream the rotor. The results of this experiment at the optimal tip speed ratio $\lambda = 6$ were used to validate the ALM and flow solver.

BT2 [18], a follow up experiment, involves two rotors placed in-line spaced three diameters apart. As in BT1, profiles are available at three locations, this time downstream the second rotor. In this paper the case where both rotors are operated at their optimal tip speeds is simulated, with $\lambda_1 = 6$ and $\lambda_2 = 4$ for the first and second rotor respectively.

2.1. Numerical scheme

LES computational fluid dynamics (CFD) simulations were performed by solving the filtered, unsteady, incompressible 3D Navier-Stokes equations with Smagorinsky turbulence closure using OpenFOAM. Second order central spatial and second order backward temporal descretization schemes are used. The PISO algorithm is used for pressure-velocity coupling and the maximum CFL values are kept at around 0.5. The boundary conditions for the wind tunnel walls are Spalding wall functions, fixed value velocity for the inlet and fixed pressure gradient for the outlet. No inlet turbulence is introduced in the domain.

The in-house ALM used in this study introduced in [19] was implemented in OpenFOAM v2.3.1 by Hunter *et al.* [20] and later transferred to version 20 06 [21]. The three steps of the ALM are briefly summarized as follows: (1) sampling of the relative flow velocity and angle of attack at each collocation point, (2) the calculation of the blade force, and (3) the imposition and smearing of the force using a kernel function. The sampling (1) here is done using the potential flow-based method described in [19]. This method samples the flow outside the force smearing region which leads to improved convergence of blade forces with time-step. The allowable time-steps using such methods are generally larger than the time-steps permitted in methods that sample the flow field at the collocation point [4, 22]. Nevertheless, the time-step used herein ensures that spurious momentum oscillations that can arise due to overly large time steps are not present, as illustrated in Figure 2. For step (2), the airfoil data were calculated using XFoil [23] as per Krogstad and Lund [24]. The anisotropic tip correction model of Wimshurst and Willden [25], which has been calibrated for a similar scale rotor as the one simulated here, is used. Finally, the smearing kernel used here is the three dimensional Gaussian kernel, used in Sørensen and Shen [22] with a kernel width of $\varepsilon = 2.5\Delta x$, as per Martínez-Tossas *et al.* [4]. The supporting structures are modelled using a volume of fluid approach introduced by Apsley *et al.* [26].

2.2. Convergence

The meshes are of Octree type. The domain size in all cases is equivalent to the wind tunnel size with a slightly elongated streamwise direction to enclose longer wakes $[L \times W \times H] =$

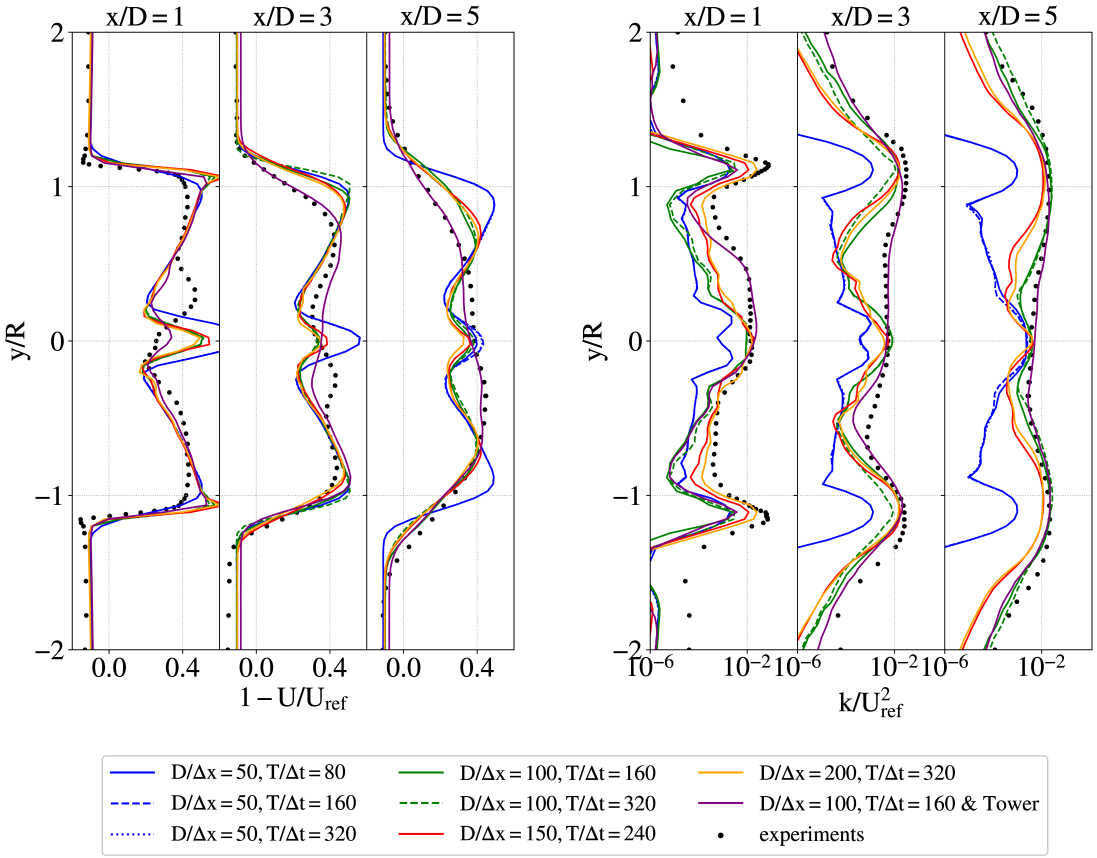

Figure 1. Blind Test 1: Horizontal profiles of mean streamwise velocity deficit (left) and turbulent kinetic energy (right) at three downstream positions x/D for varying cell sizes $D/\Delta x$ and time-steps $T/\Delta t$ and comparison with experimental data. The nacelle is modelled in all cases but the tower is only modelled in one (& Tower, purple).

$[15D \times 3D \times 2D]$ and the mesh in both cases is refined in the wake regions. The refined region for BT1 spans $[L \times W \times H] = [10D \times 1.5D \times 2D]$, centred 1 diameter upstream of the rotor and 9 downstream in the streamwise direction, and symmetrical around the center of the rotor in the other two directions. For BT2 the refined region spans $[L \times W \times H] = [13D \times 1.5D \times 2D]$, i.e., 3 diameters more than the single rotor case in the streamwise direction in order to resolve both wakes.

Independence from the mesh has been established for BT1 by simulating the rotor in four different refinement levels $D/\Delta x = 50, 100, 150, 200$, where Δx refers to the most refined cell size of each mesh. It can be seen in Figure 1 that the coarsest mesh, $D/\Delta x = 50$, under-predicts turbulence leading to limited mixing moving downstream. The case of $D/\Delta x = 100$ is very similar to the more refined cases, $D/\Delta x = 150, 200$, in terms of mean velocity, and for turbulence captures the main features even at the far wake $x/D = 5$ but slightly over-predicts turbulence at this location. The velocity and turbulence profiles for $D/\Delta x = 150$ and 200 largely agree with each other. From this comparison, it is concluded that the $D/\Delta x = 150$ simulations give a reasonable trade-off between convergence and computational cost and the data from these simulations will be used in the proceeding analysis. When it comes to comparison with the experimental data, it is important to note that all simulations model the nacelle but only

one (purple line in Figure 1) models the tower as well. This simulation agrees better with the experimental data, providing both confidence in the mesh convergence and the accuracy of the results. However, in this work we have excluded the tower for simplicity.

The effect of time-step $T/\Delta t$, where T is the rotor period, is also investigated in the same figure. Three different time-steps are investigated for the $D/\Delta x = 50$ case, and two for the $D/\Delta x = 100$. In none of the cases simulated does the time-step affect the mean velocity or turbulent kinetic energy in any wake location (Figure 1), leading to the conclusion that the largest time-step can be used for numerical efficiency.

2.3. Simulation setup

The wake data produced for DMD analysis are based on BT1 and BT2, but have been slightly adapted to ensure that the two flows are equivalent in the mean sense. In what follows, the single turbine simulation is referred to as $C1$, case 1, and corresponds to a single rotor simulation with a uniform and laminar inflow, and the two rotor simulation as $C2$, case 2.

$C2$ has the exact same set up as BT2: the upstream and downstream rotor TSRs are $\lambda_1^{C2} = 6$ and $\lambda_2^{C2} = 4$. The reference velocity for both rotors is $U_{ref} = 10$ m/s, which is also the upstream velocity of the first rotor. The upstream rotor rotates at $\omega_1^{C2} = 134\,\text{rad s}^{-1}$ and the downstream at $\omega_2^{C2} = 89\,\text{rad s}^{-1}$.

In order for the wake of $C1$ to be comparable to the wake of $C2$, the same rotational speed is ensured, i.e. $\omega^{C1} = \omega_2^{C2} = 89\,\text{rad s}^{-1}$ as well as the same levels of momentum extraction. To achieve this, it is ensured that the thrust and power produced by both rotors is the same. For this to be achieved, the U_{ref} of case $C1$ was varied until the thrust and power of the rotor matched that of the downstream rotor of $C2$. The reference velocity at $C1$ is found to be $U_{ref}^{C1} = 6.2$ m/s, with $\lambda^{C1} = 6.47$. In $C2$ azimuthal velocity variations have been introduced, and as a result the blade loads are not completely equivalent in the spanwise sense, but the overall momentum extraction in the two cases is the same. Snapshots of the instantaneous vorticity magnitude fields of the two cases, $C1$ and $C2$ are shown in Figure 2, where the wake breakdown of $C1$ and $C2$ is clearly visible.

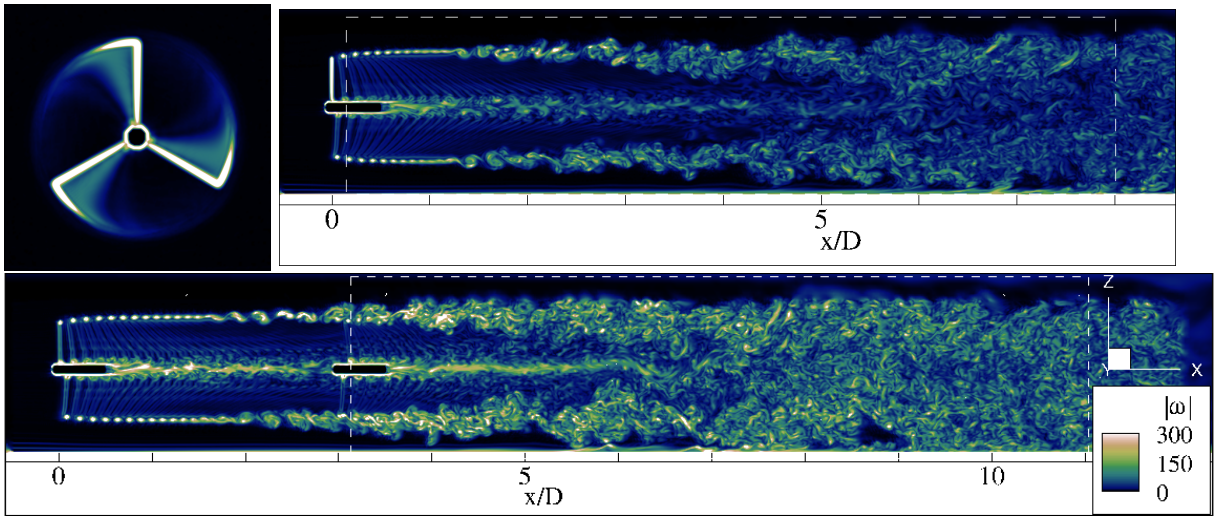

Figure 2. Upper panel: instantaneous vorticity magnitude contours for case $C1$ at the rotor plane $x = 0$ (left) and at a vertical plane through the middle of the rotor (right). Lower panel: instantaneous vorticity magnitude contours for case $C2$ at a vertical plane through the middle of the rotors. The domains where the DMD analysis is performed for the two cases are shown in white dashed lines.

3. High Order DMD

The HODMD was introduced by Le Clainche and Vega [27] and has been applied to a number of of turbulent flows including wind turbine wakes [28] and wind resource data [17]. The method combines the standard DMD with Takens' delay embedding theorem [29], leading to enhanced noise filtering properties, robustness and flexibility as well as numerical efficiency [27].

3.1. Algorithm

Applying DMD or HODMD to a spatio-temporal field $\mathbf{v}(x, y, z, t)$, which could be the fluctuating component of the velocity field of a 3D flow, results in the decomposition of Equation 1. The flow is decomposed into a sum of M complex modes $\mathbf{u}_m$, each of which is multiplied by its temporal dynamics characterized by an angular frequency ω_m and a growth rate δ_m. The modes are ranked by their real amplitude α_m.

$$\mathbf{v}(x, y, z, t_k) \simeq \sum_{m=1}^{M} \alpha_m \mathbf{u}_m(x, y, z) e^{(\delta_m + i\omega_m)t_k}, \qquad k = 1, ..., K. \tag{1}$$

In this paper, the multi-dimensional HODMD is used where, instead of two dimensional matrices, multi-dimensional tensors are used. The algorithm has two steps: in the first step, truncated high order singular value decomposition (HOSVD) is applied to the snapshot tensor in order to reduce its dimension and filter noise. The truncation is done using a user-defined error ε_1 where, r singular values σ_i are retained according to $\sigma_{r+1}/\sigma_1 \leq \varepsilon_1$. In the second step the DMD-d algorithm is applied that seeks the eigenvalues and eigenvectors of the modified Koopman matrix that is defined by modifying the initial snapshot tensor by adding d-index lagged snapshots, where d is the user-defined degree of the HODMD decomposition. The amplitudes α_m are calculated using a least-squares approach equivalent to optimized DMD [30]. The number of retained modes M in Equation 1 is calculated through a second user-defined tolerance ε_2, $\alpha_{M+1}/\alpha_1 \leq \varepsilon_2$.

3.2. Calibration

The DMD and HODMD algorithms depend on certain user-defined variables such as the SVD and DMD errors ε_1 and ε_2, the degree d, the number of snapshots K and sampling frequency f_s. It is important to ensure that the modes selected for analysis and flow characterization are robust and therefore independent from the above parameters. For this reason, mode selection in HODMD is done through a calibration process where the user-defined parameters are varied and multiple HODMD decompositions are performed. The resulting modes are compared with each other in terms of frequency and shape in order to identify clusters of modes that characterize a robust structure. Those clusters must have similar frequency, that according to Le Clainche *et al.* [31] can be within a specified range $|f_{m,i} - f_{m,j}| < \epsilon$ where ϵ is an order of magnitude larger than the largest ε_1 involved in the calibration. The shape of modes is also checked by means of projection of one mode onto another $|\mathbf{u}_{m,i} \cdot \mathbf{u}_{m,j}| > 0.9$. If modes satisfy both conditions, then they belong to the same cluster. A cluster is robust if it contains modes from 75% of the decompositions performed as per [31].

3.3. Data collection

For the DMD analysis in this paper, spatio-temporal data are extracted from the simulations $C1$ and $C2$ described in Section 2.3. Although the CFD mesh has a cell size of $D/\Delta x = 100$ in the wake region, the DMD mesh has a cell size of $D/\Delta x = 50$ due to the large memory requirements of the analysis. The 3D DMD domain spans from $0.1D$ downstream of the rotor of interest (that is, the single rotor of $C1$ and the downstream rotor in $C2$) to $8D$ downstream as indicated by the white dotted rectangles in Figure 2 and has a $1.5D \times 1.5D$ square cross section in the YZ plane,

centered on the hub. The frequency of data collection f_s corresponds to 10 snapshots per period. This gives a Nyquist frequency of $5/T$. It is acknowledged here that prior studies have indicated the presence of higher frequencies in wind turbine wakes ([10, 9]). Nonetheless, the present investigation is primarily concerned with lower frequencies. The number of snapshots in both cases is $K = 300$ which means that data are collected for 30 periods and therefore the minimum detectable frequency, $1/(30T)$, is much smaller than the rotor frequency. The sampling frequency and duration used here are similar to Debnath *et al.* [13]. This choice provides a satisfactory trade-off between memory requirements and frequency range. Various sets of (K, f_s) were tested in order to ensure that our conclusions not depend on those parameters. This investigation has been omitted from this paper for brevity.

4. HODMD of two flows: a single and a downstream rotor wake

4.1. Dependence of the results on user-defined parameters

All cases have been calibrated using the same user-defined variables, following Le Clainche *et al.* [31]. 90% of the highest amplitude modes are visualized in the frequency-amplitude plots of Figure 3. The circled modes, are the most robust ones according to the criteria detailed in section 3 and are therefore the ones that describe coherent structures that exist in the flow.

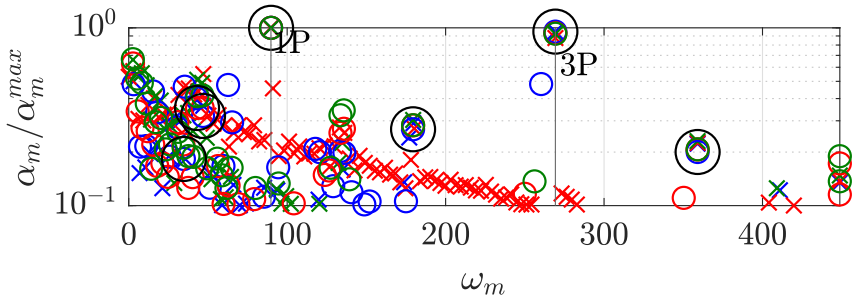

Figure 3. HODMD calibration for $C1$: Angular frequency ω against amplitude normalized by the maximum value α, for different SVD tolerances ε_1 and degrees d. The crosses indicate $\varepsilon_1 = 0.05$ and the circles, $\varepsilon_1 = 0.01$. Blue, red and green colours correspond to degrees 125, 93 and 75 respectively for $K = 300$ snapshots. The black circles correspond to clusters of modes that appear in at least 75% of the decompositions performed. $1P$ and $3P$ frequencies are noted, based on the rotation frequency $\omega^{C1} = \omega_2^{C2} = 89\,\text{rad s}^{-1}$.

In addition to the dependence on user-defined parameters discussed above, the DMD modes may also exhibit sensitivity to the numerics of the CFD simulations, particularly in situations where the inflow is laminar, such as case $C1$. For this reason, investigations of tip vortex interactions in wind turbine wakes [9, 11] explicitly introduce known disturbances to the flow in order to eliminate the uncertainty arising from the unknown numerical perturbations. However, the present study aims to compare two distinct flow cases that are subjected to the same numerical treatment, similar to [13, 14]. Consequently, the primary focus of this study will be to analyze the differences between the cases $C1$ and $C2$, in order to minimize the influence of those numerical perturbations. It is important to note that the absence of explicit perturbations in this study represents a limitation, and as a result, only qualitative conclusions are drawn.

4.2. HODMD of a single rotor wake

The most robust modes selected for case $C1$ are identified in Figure 3. The highest amplitude mode has a frequency of $\omega_{1P} = 89\,\text{rad s}^{-1}$. The 3P mode identified at $\omega_{3P} = 3\omega_{1P} = 269\,\text{rad s}^{-1}$ also ranks very highly. Further robust and high amplitude modes are found at lower than $1P$

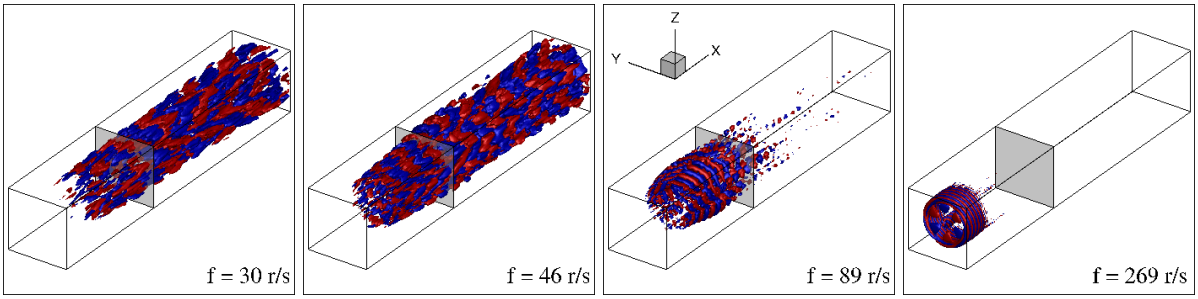

Figure 4. Isosurfaces of the streamwise real part of three of the most robust dynamic modes for case $C1$. The x-surface shaded in the top figures is located at $x/D = 3$, where the second rotor in $C2$ is situated.

frequencies. The remaining of the robust modes are harmonics or modulation of the above mentioned dominant modes and are not discussed further.

The $1P$ mode is very active in the transition region between $x/D = 1 - 3$ (Figure 4) and mainly occupies the edge of the wake, around $r = R$, where r is the spanwise coordinate and R the rotor radius. When compared with the vorticity magnitude contour in Figure 2 it is clear that at $x/D \approx 1.2$ the tip vortex instability is triggered and the structures emerging from it persist until $x/D = 3$, where some mixing with more complex structures occurs. This mode resembles in shape and frequency the $1P$ mode identified in the blade-resolved wakes of Sun *et al.* [10], indicating that some of the dynamics emerging from ALM simulations are similar to the ones identified in higher-fidelity rotor representations. However, higher resolution simulations with explicit perturbations could potentially reveal additional frequencies in this region of tip vortex breakdown, such as mutual-inductance instability of merging tip-vortices [9] of various wavelengths and frequencies, but these are not evident in our computations.

The $3P$ mode corresponds to the tip-vortex structures that are only significant in the near wake. The tip structures are even more confined at an annular ring at $r = R$ and are also visible in the instantaneous vorticity magnitude contour of Figure 2. The $3P$ mode is typically found in all DMD analysis of wind turbine wakes [13, 14].

The lower frequency modes are more spatially persistent, characterizing the region starting from $x/D = 1.5$ and extending to the end of the domain. The appearance of robust low frequency modes, at frequencies approximately 10 times lower than the blade passing frequency are also evident in the DMD decomposition of a stand-alone rotor in laminar flow of [14], although the tower was also included in that case. In the same study, the $3P$ mode was also evident, but no $1P$ modes were observed, potentially due to the interaction with the tower.

Overall, moving from the near to the far wake of a single rotor, three types of structures of decreasing frequency and increasing radial width are identified (Figure 4). The near-wake tip vortices start off as very predictable helical structures emanating from the blade tips at $3P$ and dominant at $x/D < 1$. A $1P$ frequency, with slightly greater radial extent but still predominantly near the tip radius, is associated with the breakdown of the tip vortices and characterizes the transitional wake at $1 < x/D < 3$. This is also visible in Figure 2 in the instantaneous vorticity magnitude. Finally, structures with $\omega_m < 89\,\mathrm{rad\ s^{-1}} \simeq 0.2P - 0.4P$, are associated with the transitional and far wake.

4.3. HODMD of a downstream wake and comparison with the single wake

In order to discuss the dynamic modes of case $C2$, the frequencies incident at the second rotor of $C2$ are first characterized. For this, HODMD has been performed in the same domain as the one in the white box of the lower panel of Figure 2 but in the absence of the second rotor.

Essentially, this reveals the far wake modes of the upstream rotor in $C2$ which is operating at $\lambda = 6$. These modes, following the discussion in Section 4.2, are spatially persistent and occur at low frequencies and their modal shape is similar to the low frequency modes of Figure 4. Those modes are referred to as the background (BG) flow.

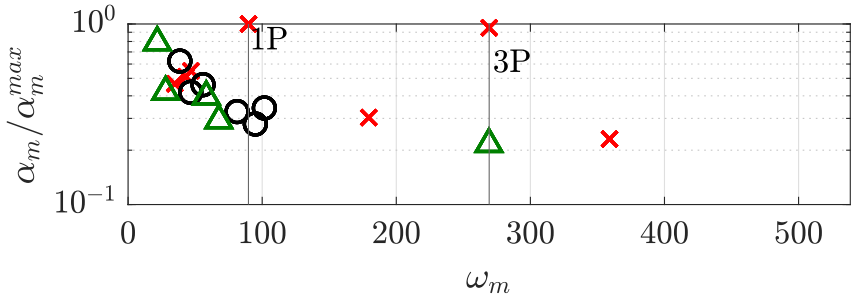

Figure 5. The most robust modes for case $C1$ (×), $C2$ (△) and BG of $C2$ (O). All modes shown here are a result of a calibration that employs the same parameters as the ones used in Figure 3. Only the modes that are independent of the user defined parameters are presented.

A comparison of the dynamics of $C1$, $C2$, and BG is presented in Figure 5. It can be seen that, when a rotor operates in the wake of an upstream rotor, the lower frequencies of the background flow become dominant. The only high frequency identified is the $3P$ frequency, that occurs at notably lower amplitudes compared to $C1$. All other frequencies are below $1P$.

The prevalence of the background low frequencies over the "endogenous dynamics" as characterized by De Cillis *et al.* [14] have been identified in a similar case where atmospheric turbulence with a turbulence intensity less than 10% was imposed on the flow. There, the authors observed that when background turbulence is imposed upstream a rotor, high frequency modes are not selected by the sparsity-promoting DMD and the flow is characterized by the low frequencies. Similarly in the present work, in $C2$ the average turbulence intensity at the rotor plane is less than 8% (as indicated in Figure 1) and only one higher ($> 1P$) frequency is present at a low amplitude.

5. Conclusions

In this work the wake merger of two wind turbines in-line is under consideration, with the upstream wake having broken down to turbulence. Two wakes, a laminar inflow stand-alone rotor wake and a downstream wake that operates in the turbulent wake of an upstream rotor, are simulated using ALM-LES and validated using published experimental data. The datasets are investigated using HODMD. The two sets of resulting modes are compared in order to investigate the similarities and differences between the combined wake and the single turbine wake.

The dominant modes of the laminar inflow case generally consist of both high and low frequencies. The modal shapes agree with others found in literature giving confidence in both the decomposition method and simulation results.

When a rotor operates in the turbulent wake of an upstream turbine, the high frequency content identified in the laminar case is highly suppressed meaning that the background structures that characterize the far-wake of the upstream rotor are more dynamically persistent than the higher frequencies identified in the laminar case, a conclusion also drawn by [14] for atmospheric inflow turbulence. This conclusion qualitatively shows that within the wind farm, the rotor geometry and rotation might be less important than when compared to the stand-alone case, suggesting that other turbine modelling approaches, such as the ADM could also adequately capture important far-wake dynamics.

This work has developed a framework for the analysis of wind turbine wakes using HODMD that can be used for the exploration of other types of wakes as well as the development of reduced order models. The framework has been used to explore how the dynamics of a wind turbine wake are affected when it is operating within an upstream wake. HODMD at higher resolution data, with explicitly imposed perturbations as well as the simulation of different turbine spacings and layouts or modelling of the tower are necessary to generalize the conclusions and are a direction for future study.

Acknowledgments

The work has been performed under the Project HPC-EUROPA3 (INFRAIA-2016-1-730897), with the support of the EC Research Innovation Action under the H2020 Programme; in particular, the authors gratefully acknowledge the computer resources and technical support provided by the Barcelona Supercomputing Center (BSC).

The first author would also like to greatly acknowledge RWE Renewables and the Department of Engineering Science of the University of Oxford for the awarded studentship and thank the University of Oxford's Advanced Research Computing (ARC) facility for proving access to HPC resources in support of this work.

The authors are also grateful to the anonymous reviewers for their insightful input.

References

[1] Barthelmie R J, Hansen K, Frandsen S T, Rathmann O, Schepers J G, Schlez W, Phillips J, Rados K, Zervos A, Politis E S and Chaviaropoulos P K 2009 *Wind Energy* **12** 431–444
[2] El-Asha S, Zhan L and Iungo G V 2017 *Wind Energy* **20** 1823–1839
[3] Krogstad P and Eriksen P E 2013 *Renewable Energy* **50** 325–333
[4] Martínez-Tossas L A, Churchfield M J and Leonardi S 2015 *Wind Energy* **18** 1047–1060
[5] Jensen N 1983 A note on wind generator interaction. Tech. rep. Risø National Laboratory. Risø-M, No. 2411
[6] Bastankhah M and Porté-Agel F 2014 *Renewable Energy* **70** 116–123
[7] Vogel C R and Willden R H J 2020 *Wind Energy* **23** 593–607
[8] VerHulst C and Meneveau C 2014 *Physics of Fluids* **26** 025113
[9] Sarmast S, Dadfar R, Mikkelsen R F, Schlatter P, Ivanell S, Sørensen J and Henningson D 2014 *Journal of Fluid Mechanics* **755** 705–731
[10] Sun C, Tian T, Zhu X c, Ouyang H and Du Z 2021 *Energy* **227** 120418
[11] Kleine V G, Kleusberg E, Hanifi A and Henningson D S 2019 *Journal of Physics: Conference Series* **1256** 012015
[12] Bastine D, Witha B, Wächter M and Peinke J 2015 *Energies* **8** 895–920
[13] Debnath M, Santoni C, Leonardi S and Iungo G 2017 *Philosophical Transactions of The Royal Society A Mathematical Physical and Engineering Sciences* **375** 20160108
[14] De Cillis G, Cherubini S, Semeraro O, Leonardi S and de Palma P 2022 *Renewable Energy* **183** 601–616
[15] Hamilton N, Viggiano B, Calaf M, Tutkun M and Cal R B 2018 *Wind Energy* **21** 373– 390
[16] Le Clainche S and Ferrer E 2018 *Energies* **11** 566
[17] Le Clainche S, Lorente L S and Vega J M 2018 *Energies* **11** 543
[18] Pierella F, Åge Krogstad P and SL 2014 *Renewable Energy* **70** 62–77
[19] Schluntz J and Willden R H 2015 *Wind Energy* **18** 1469–1485
[20] Hunter W, Nishino T and Willden R H J 2014 9th OpenFOAM Workshop (Zagreb, Croatia)
[21] 20 06 OpenFOAM ESI available https://www.openfoam.com/ [accessed 2022]
[22] Sorensen J N and Shen W Z 2002 *Journal of Fluids Engineering* **124** 393–399
[23] Drela M 1989 Xfoil v.6.97 available http://web.mit.edu/drela/Public/web/xfoil/ [accessed 2022]
[24] Krogstad P and Lund J 2012 *Wind Energy* **15** 443–457
[25] Wimshurst A and Willden R H J 2017 *Wind Energy* **20** 1515–1528
[26] Apsley D, Stallard T and Stansby P 2018 *Journal of Ocean Engineering and Marine Energy* **4** 259–271
[27] Le Clainche S and Vega J M 2017 *SIAM Journal on Applied Dynamical Systems* **16** 882–925
[28] Le Clainche S, Mao X and Vega J M 2019 *Wind Energy* **22** 922–931
[29] Takens F 1981 *Dynamical Systems and Turbulence, Lecture Notes in Mathematics* **898** 366–381
[30] Chen K, Tu J and Rowley C 2012 *Journal of Nonlinear Science* **22** 887–915
[31] Le Clainche S, Izbassarov D, Rosti M, Brandt L and Tammisola O 2020 *Journal of Fluid Mechanics* **888** A5